

# High Performance Proprioceptive Fiber Actuators Based on Ag Nanoparticles-Incorporated Hybrid Twisted and Coiled System

Seungbeom Noh, Jinho Kim, Hwajoong Kim, Muguen Lee, Namjung Kim, Hyeji Ryu, and Jaehong Lee\*

Thermally driven fiber actuators are emerging as promising tools for a range of robotic applications, encompassing soft and wearable robots, muscle function restoration, assistive systems, and physical augmentation. Yet, to realize their full potential in practical applications, several challenges, such as a high operational temperature, incorporation of intrinsic self-sensing capabilities for closed-loop feedback control, and reliance on bulky, intricate actuation systems, must be addressed. Here, an Ag nanoparticles-based twisted and coiled fiber actuator that achieves a high contractile actuation of pprox36% is reported at a considerably low operational temperature of pprox83 °C based on a synergistic effect of constituent fiber elements with low glass transition temperatures. The fiber actuator can monitor its contractile actuation in real-time based on the piezoresistive properties inherent to its Ag-based conductive region, demonstrating its proprioceptive sensing capability. By exploiting this capability, the proprioceptive fiber actuator adeptly maintains its intended contractile behavior, even when faced with unplanned external disturbances. To demonstrate the capabilities of the fiber actuator, this study integrates it into a closed-loop feedback-controlled bionic arm as an artificial muscle, offering fresh perspectives on the future development of intelligent wearable devices and soft robotic systems.

S. Noh, J. Kim, H. Kim, M. Lee, H. Ryu, J. Lee Department of Robotics and Mechatronics Engineering DGIST

333, Techno jungang-daero, Hyeonpung-eup, Dalseong-gun, Daegu 42988, Republic of Korea

E-mail: jaelee@dgist.ac.kr

N. Kim

Department of Mechanical Engineering

Gachon University

1342, Seongnam-daero, Sujeong-gu, Seongnam-si, Gyeonggi-do 13120, Republic of Korea



The ORCID identification number(s) for the author(s) of this article can be found under https://doi.org/10.1002/smll.202309429

© 2024 The Authors. Small published by Wiley-VCH GmbH. This is an open access article under the terms of the Creative Commons Attribution License, which permits use, distribution and reproduction in any medium, provided the original work is properly cited.

DOI: 10.1002/smll.202309429

#### 1. Introduction

Soft actuators have recently attracted significant attention in the field of robotics owing to their remarkable advantages, such as exceptional mechanical compliance, [1,2] high adaptability to objects with various shapes,[3,4] lightweight,[5-7] and costeffective fabrication.<sup>[8,9]</sup> Among the diverse types of soft actuators, fiber-based soft actuators have rapidly emerged in a variety of applications, including robotic garments, [10,11] smart textiles,<sup>[12–17]</sup> wearable robots,<sup>[18–20]</sup> and biomedical applications,[21-24] thanks to their unique fibrous structure. Thermally driven twisted and coiled polymer actuators (TCAs), created by imparting a high degree of twist into polymeric fibers, represent a widely developed type of fiber-based soft actuator that possesses lowdriving power,<sup>[25–27]</sup> cost-effectiveness,<sup>[28–30]</sup> substantial work output,[31,32] and low thermal hysteresis.[33-35] These TCAs can effectively generate a significant amount of contracting actuation by leveraging the anisotropic thermal coefficient of the constituent polymeric fibers.[36,37] Haines et al.[34] presented high-performance

artificial muscles using thermally driven TCAs fabricated using nylon 6,6 polymeric fibers. Although the developed TCAs achieved impressive actuation performance with over 30% contraction, their operation requires a high working temperature exceeding 240  $^{\circ}$ C. The high working temperature of the fiber actuators considerably limits their applications, such as textile-based wearable robots and biomedical devices, which are highly vulnerable to high temperatures.

To address the limitations associated with the high operating temperatures of previous thermally driven TCAs, alternative polymeric fibers with lower glass transition temperatures have been used to develop fiber actuators that operate at lower temperatures. Hiraoka et al. [38] developed power-efficient fiber actuators using thermally driven TCAs fabricated from linear low-density polyethylene (LLDPE) fibers. While these fiber actuators could be operated at a lower temperature of  $\approx\!90$  °C, their contractile actuation decreased to  $\approx\!23\%$  due to the inherently poorer negative thermal expansion properties compared to nylon-based fiber





www.small-journal.com

actuators.[34] In addition, the heating wire,[39-41] used as an external heat source for Joule heating of the fiber actuators, could lead to nonuniform heat distribution along the fiber actuators. potentially resulting in long-term degradation of the actuator's performance. Yang et al.[42] reported spandex-based twisted and coiled fiber actuators (STCAs) with high actuating performance and a low operating temperature. The STCAs exhibited a high tensile stroke of 30% at a relatively low temperature of 80 °C based on the low glass transition temperature of polyurethanebased spandex fibers. Nevertheless, the necessity for an external heat source, such as a heating gun, leads to bulky, heavy, and complex system configurations. Furthermore, the inherent severe thermal softening property of spandex fibers could substantially compromise their thermal stability, particularly over long-term use of such thermally driven fiber actuators. To overcome the limitations of previous fiber actuators, a hybrid structure of TCAs has also been explored by combining two types of polymeric fibers into a single actuator system. Kim et al.<sup>[43]</sup> presented hybrid TCAs composed of spandex fibers wrapped around twisted and coiled nylon fibers, which were coated with a thin layer of silver (Ag). These hybrid TCAs could be operated by Joule heating generated from the Ag coating layer when external voltage was applied, thereby eliminating the need for any bulky external heat source. Moreover, the poor thermal stability inherent in spandex fibers was mitigated by combining thermally stable nylon fibers in the actuators. However, the spandex fiber, fully covering the Ag-coated nylon fibers responsible for generating Joule heating, could significantly impede the heat dissipation of the actuators. This could negatively affect the natural cooling and relaxation processes of the actuators. Additionally, these hybrid fiber actuators lack the real-time self-sensing capability essential for feedback control of the actuator system. Feedback control, which is typically achieved through sensor integration, is fundamentally essential for soft actuators for reliable operation in dynamic environments and practical applications. In this regard, conventional rigid-type sensing components, including laser distance sensors (LDS) and linear encoders, have been mainly employed for fiber actuator systems.[44,45] However, the integration of such bulky and rigid sensing components severely exacerbates the overall complexity, bulkiness, and weight of the system. While there is a strong desire to develop a fiber actuator that simultaneously addresses the limitations of previous TCAs such as high operating temperatures, limited actuation performance, bulky external heat source, poor heat dissipation behavior, and a lack of self-sensing capability, it remains challenging to effectively integrate the desired performance into a fiber actuator.

In this article, we introduce an Ag nanoparticles (AgNPs)-based fiber actuator that simultaneously features its high contractile actuation, low operation temperature, elimination of an external heat source, fast cooling time, and proprioceptive sensing capability (Figure S1, Supporting Information). This fiber actuator was realized by incorporating a large amount of AgNPs into a non-conductive hybrid TCA made of polyethylene (PE) and polyurethane (PU) fibers. The actuator achieves a high contractile actuation of  $\approx 36\%$  at a notably low operation temperature of  $\approx 83$  °C. Furthermore, it displays rapid heat dissipation under natural cooling and retains its stability over 100 actuation cycles. We develop an analytical expression and numerical model to corroborate the rapid heat dissipation, attributing it to the Ag-rich region

within the fiber. Notably, the contractile actuation of the fiber actuator can be self-monitored in real-time by measuring changes in its electrical resistance. Based on this proprioceptive sensing, the fiber actuator efficiently maintains its targeted actuation levels even under unintended external loads. We demonstrate that the presented fiber actuator can be applied to develop a feedback-controlled electrothermal artificial muscle, efficiently operated at a low operational temperature.

#### 2. Result and Discussion

## 2.1. Structural Design and Working Principle of Proprioceptive Fiber Actuator

We designed a high-performance, self-sensing hybrid fiber actuator that operates at low temperatures, using non-stretchable core fibers and highly conductive, stretchable fibers. Figure 1a shows a schematic illustration of the structure of the self-sensing hybrid fiber actuator. The fiber actuator comprises two polyethylene (PE)-based core fibers and several stretchable and conductive fibers made from composites of Ag nanoparticles (AgNPs) and an elastomeric fiber scaffold. These stretchable, conductive fibers fully wrap around the core fibers in a twisted and coiled helical structure. The fabrication process of our fiber actuators consisted of two main steps: 1) the fabrication of non-conductive hybrid TCAs using the PE core fibers and bare elastomeric fibers, and 2) the incorporation of AgNPs into the elastomeric fibers in the non-conductive TCAs for endowing electrical conductivity to the fiber. Here, commercialized polyurethane (PU)-based stretchable fibers were used as the elastomeric fiber scaffold for the hybrid TCAs. To fabricate the non-conductive hybrid TCAs, two strands of PE fiber were twisted together with several strands of pre-stretched PU fibers and secured using a distance holder (Figure 1b; Figure S2a, Supporting Information). During the twisting process, the PU fibers fully wrapped around the PE core fibers (Figure S2b, Supporting Information). The twisted PE and PU fibers were then coiled by rotating them under a coiling load, resulting in the formation of non-conductive hybrid TCAs (Figure 1b; Figure S2c, Supporting Information). The hybrid TCAs were then annealed at a high temperature of 150 °C and cooled in ambient air to prevent undesired untwisting behavior and reduce the spring force of the TCAs (Figure S3, Supporting Information). The fabricated non-conductive hybrid TCAs efficiently maintained their uniformly coiled structure, even in the absence of an external holder that is typically required to counteract the inherent torsional forces of TCAs and prevent untwisting (Figure S4, Supporting Information). To impart electrical conductivity to the non-conductive hybrid TCAs, a large amount of AgNPs was incorporated into the PU fibers wrapped around the PE core fibers within the TCAs. This was achieved by absorbing Ag+ ions into the PU fibers and subsequently reducing the absorbed Ag+ ions into metallic AgNPs within the fibers, as previously reported (Figure S5, Supporting Information).[46] Figure 1d presents a photograph of the fabricated AgNPs-based conductive hybrid TCAs, illustrating the colour change of the hybrid TCAs due to the AgNPs on their surface. Typical scanning electron microscopy (SEM) images of the AgNPs-based conductive hybrid TCAs reveal a dense coating of AgNPs. Moreover, the images show that the twisted and coiled structure of the actuator



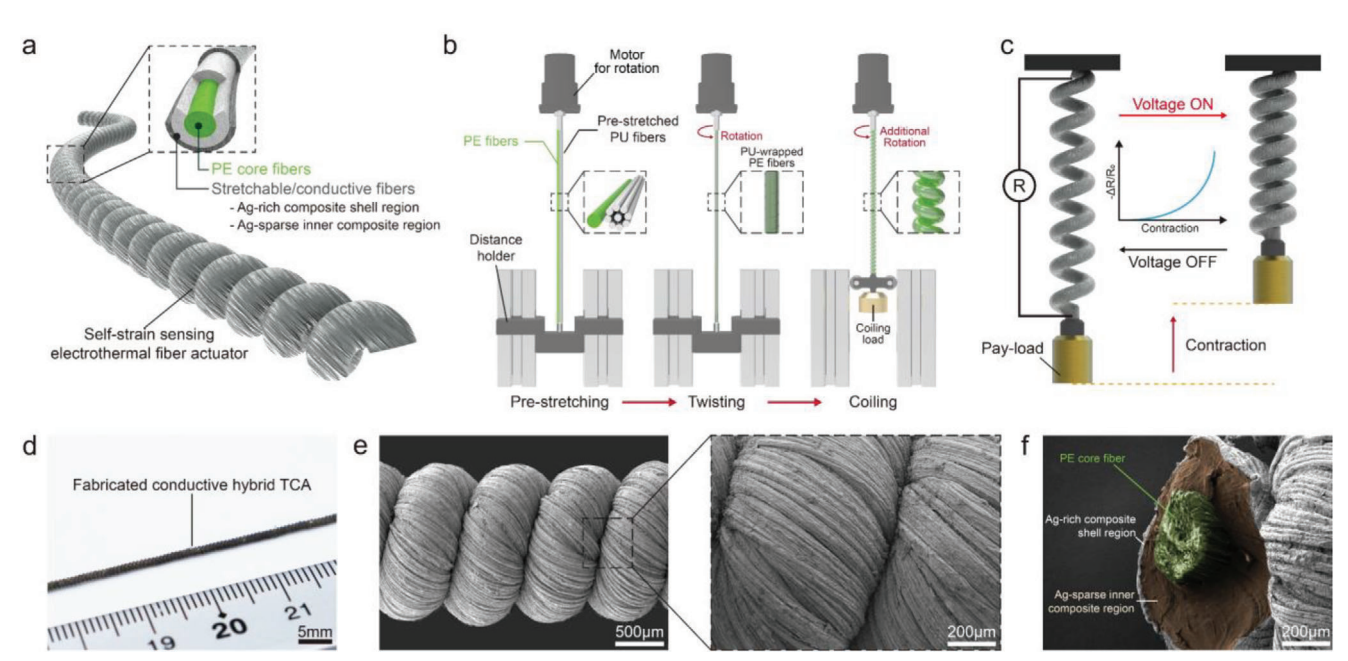


Figure 1. a) Schematic illustration of a proprioceptive fiber actuator, a conductive hybrid TCA composed of the PE core fiber and AgNPs-based conductive PU fibers. The cross-sectional view (inset) shows that the outer region, associated with the conductive PU fibers, can be divided into two distinct sections: the Ag-rich composite shell and the Ag-sparse inner composite region. b) Fabrication process for a non-conductive hybrid TCA using the PE core fiber and pre-stretched PU fibers. c) Schematic illustration showing the contractile actuation of the fiber actuator under an applied external voltage and the corresponding change in its electrical resistance. d) Photograph of the fabricated proprioceptive fiber actuator. e) Typical SEM images of the surface of the fiber actuator, showing the twisted and coiled structure of the actuator. f) Cross-sectional SEM image of the fiber actuator. The actuator comprises a PE core fiber (highlighted in green) and Ag-sparse inner composite region (highlighted in brown), and an Ag-rich shell composite region.

remains intact despite the incorporation of a substantial quantity of AgNPs through the intensive chemical reaction (Figure 1e; Figure S6, Supporting Information). Due to the gradual absorption of Ag+ ions, the AgNPs incorporation process led to the formation of two distinct regions within the PU fibers wrapped around the core fiber in the hybrid TCAs: an Ag-rich composite shell and an Ag-sparse inner composite region (Figure 1a,f).[47] These two regions with different AgNP concentrations were clearly identified in the Energy-Dispersive X-ray Spectroscopy (EDS) image of the cross-section of the fiber actuator (Figure \$7, Supporting Information). The Ag-rich composite shell region within the PU fibers is densely concentrated with AgNPs, which form tight connections between each other, resulting in high electrical conductivity. Based on the electrical contact between the densely distributed AgNPs within the proprioceptive fiber actuator, the fiber actuator exhibits a high electrical conductivity of  $\approx$ 11,891 S cm<sup>-1</sup>. The dense concentration of AgNPs in the shell region could result from the diffusion of internal Ag ions onto the surface of the fiber actuator during the reduction process.<sup>[48]</sup> Despite behaving electrically similar to a bulk Ag layer due to the high concentration of incorporated AgNPs, the shell region successfully maintains exceptional mechanical stability and flexibility, thanks to its elastomeric matrix.[47] The Ag-sparse inner composite region in the PU fiber layer features a lower concentration of AgNPs relative to the Ag-rich composite shell region.

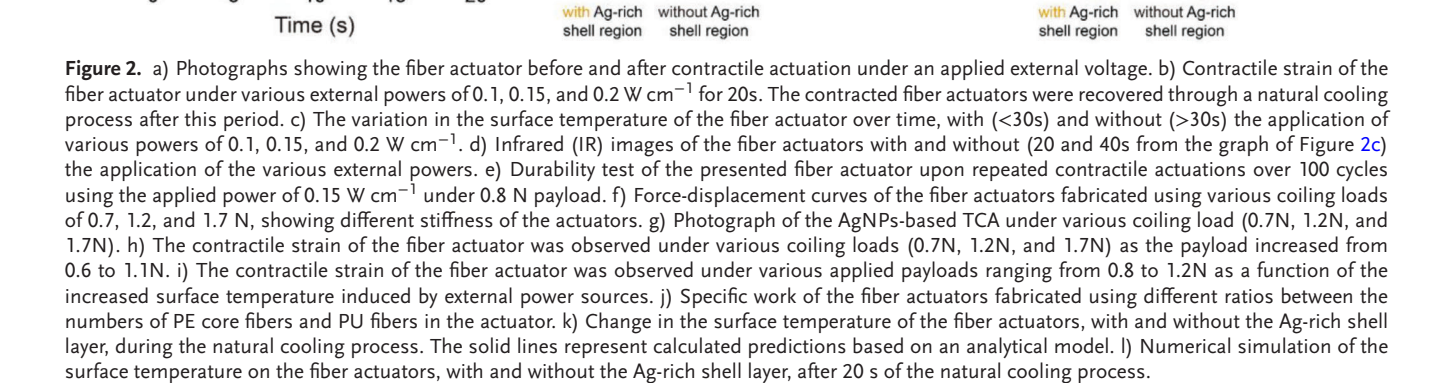
Based on the conductive Ag-rich composite shell region, the conductive hybrid TCAs can be efficiently actuated through Joule heating evenly generated across the TCAs when an external voltage is applied (Figure 1c). As a result, the conductive hybrid TCAs

can operate without the need for any bulky external heat source, greatly simplifying the entire system. Furthermore, the contractile actuation of the conductive hybrid TCAs can be monitored in real-time by measuring the electrical resistance of the conductive PU fibers within the TCAs. The electrical resistance of the conductive hybrid TCAs changes effectively in relation to the contraction of the TCAs, attributable to the cracking process of the Ag-rich shell region within the TCAs during actuation. This proprioceptive sensing capability of the conductive hybrid TCAs enables closed-loop feedback control of the actuator system. In this study, we refer to the AgNPs-based conductive hybrid TCAs with self-sensing capability, fabricated using the PE core fibers and conductive PU fibers, as a proprioceptive fiber actuator.

### 2.2. Electrothermal Actuation Performance of the Proprioceptive Fiber Actuator

The proprioceptive fiber actuator, elongated by an isobaric payload, can efficiently contract under external electrical voltage (Figure 2a; Video S1, Supporting Information). This voltage generates Joule heat, primarily in the Ag-rich shell region of the actuator. The increased temperature from the Joule heat causes radial expansion of the twisted and coiled structure in the fiber actuator, driving contractile actuation. Figure 2b displays the contractile actuations of the fiber actuator, fabricated using a coiling load of 1.2 N, under an isobaric payload of 1 N with various applied electrical powers of 0.1, 0.15, and 0.2 W cm $^{-1}$ . We defined the contractile strain of the fiber actuator as  $\epsilon = (L_{\rm initial}, L_{\rm final})/L_{\rm initial}$ , where

**SCIENCE NEWS** 



Cooling

Ag-rich shell Polyurethane
Polyethylene

60

50

40

30

0

5

10

15

20

31.0 °C 30.3 °C

29.7 °C

29.0 °C

28.3 °C 27.7 °C

27.0 °C



www.small-journal.com

 $L_{initial}$  and  $L_{final}$  represent the longitudinal lengths of the loaded fiber actuator without and with applied power, respectively. The contractile strain of the fiber actuator increased with higher electrical power, as increased temperature caused further radial expansion and contractile actuation. Owing to Joule heating in the Ag-rich shell region, the surface temperature of the fiber actuator increased to  $\approx$ 37.2,  $\approx$ 59.2, and  $\approx$ 80.5 °C with applied powers of 0.1, 0.15, and 0.2 W cm<sup>-1</sup>, respectively (Figure 2c). The fiber actuator heated uniformly across its entire length under applied external power, thanks to the consistent electrical properties of the Ag-rich shell (Figure 2d). This uniform heating ensured stable and reproducible actuator operation. Exhibiting high stability, the fiber actuator consistently maintained stable contractile actuation without significant degradation during an intensive 100-cycle test at 0.15 W cm<sup>-1</sup> with an isobaric payload of 0.8 N, thus demonstrating the high durability of the fiber actuator (Figure 2e).

The actuation performance of the fiber actuator was further investigated by examining the stiffness of fiber actuators fabricated using various coiling loads, as shown in Figure 2f. As the coiling load applied during the fabrication of the fiber actuator increased from 0.7 to 1.2 N, the stiffness of the fiber actuator correspondingly increased from 0.105 to 0.132 N mm<sup>-1</sup>. This increase in stiffness is attributed to an increase in the bias angle of the actuator fabricated with a greater coiling load (Figure 2g; Figure S8, Supporting Information).

An insufficient bias angle and low stiffness could result in excessive elongation of the fiber actuator under payloads, leading to a degradation in the contractile strain of the actuator. Conversely, an excessively large bias angle and high stiffness of the fiber actuator might prevent moderate elongation under payloads, which could also reduce the contractile actuation. Figure 2h shows the contractile strain of various fiber actuators fabricated using different coiling loads of 0.7, 1.2, and 1.7 N in response to diverse isobaric payloads ranging from 0.6 to 1.1 N. While the contractile strain of the fiber actuator decreased as the applied payload increased, the actuator fabricated with a coiling load of 1.2 N achieved a high contractile actuation of ≈36% with a 0.7 N payload under a remarkably low operating temperature of ≈83 °C. While the operating temperature of the proprioceptive fiber actuator might pose a challenge for application in wearable devices, the presented fiber actuator exhibits a lower operating temperature than that of previously reported actuators (Table S1, Supporting Information). Therefore, we expected that the proprioceptive fiber actuator could be readily applied to wearable devices by incorporating an additional buffer fabric, which could help avoid direct contact between the fiber actuator and human skin. Our outstanding performance, including low operating temperature, contractile actuation, specific work, fast cooling time, and contraction rate, outperforms those of previously reported fiber actuators (Table S1, Supporting Information). This achievement is due to the synergistic hybrid structure of the PU and PE fibers, both of which demonstrate high performance at low operating temperatures. Owing to the higher glass transition temperature of HDPE compared to the operating temperature of the fiber actuator, our proprioceptive fiber actuator demonstrates enhanced thermal robustness, thereby significantly improving its long-term stability. [49] Given its high performance, the fiber actuator displayed a strong linear relationship between its contractile actuation and surface temperature (Figure 2i).

Additionally, the specific work of the fiber actuator was investigated in relation to different ratios of PE core to PU fibers in the actuators (Figure 2j; Figure S9, Supporting Information). The specific work of the actuator, typically defined as the amount of work performed per unit mass, increased as the proportion of PU fibers in the fiber actuator increased. Although the high density of PE fibers could potentially compromise the specific work of the fiber actuator, the proprioceptive fiber actuator could ensure high thermal stability owing to the PE fibers. This positive correlation can be attributed to the lightweight nature of the PU fibers, which results in higher specific work for PU fiber-based actuators compared to HDPE fiber-based ones.[38,42] The fiber actuator fabricated using 20 PU fibers and 2 HDPE fibers (a 10:1 ratio) with a coiling load of 1.2 N demonstrated a high specific work of 650.4 J kg<sup>-1</sup> under a payload of 1N and an applied power of 0.2 W cm<sup>-1</sup> (Figure 2j; Figures S10 and S11, Supporting Information).

In addition to high actuation performance at a low operating temperature, the presented fiber actuator is capable of more efficiently dissipating heat in an ambient air environment during the cooling step. The Ag-rich shell layer on the outermost region of the fiber actuator possesses a higher natural convection coefficient than the bare PU fibers. The enhanced natural convection coefficient of the fiber actuator is the result of the elevated surface roughness caused by the incorporation of AgNPs. [50,51] This property facilitates faster heat dissipation without the need for an external cooling system. The proposed fiber actuator exhibited a natural cooling time that is  $\approx$ 40% faster, cooling down to pprox36.5 °C, a temperature similar to average human skin, when compared to non-conductive hybrid TCAs without the Ag-rich shell region (Figure 2k). An analytical model for the efficient heat dissipation of the fiber actuator was established based on Newton's cooling law, detailed in the Supporting Information. Calculated surface temperatures of the actuators, both with and without the Ag-rich shell region, were found to excellently align with the experimental results (Figure 2k). Moreover, a finite element model was created to simulate the surface temperature of the fiber actuator after 20 seconds of natural cooling, as shown in Figure 21. The simulated surface temperature of the actuator aligns well with experimental results, confirming the fast natural cooling property of the fiber actuator with the Ag-rich shell region (Figure \$18, Supporting Information).

#### 2.3. Proprioceptive Sensing Capability of the Fiber Actuator

The stretching and contraction of the proprioceptive fiber actuator can be monitored in real-time by measuring its electrical resistance. Predominantly determined by the AgNPs-based conductive PU fibers within the actuator, the electrical resistance varies in accordance with both tensile and contractile strain. In particular, the AgNPs-based conductive PU fibers within the actuator can serve as a strain sensor based on the cracking process of the Ag-rich shell region under external strain, as previously reported. When the fiber actuator is subjected to tensile strain, the coiled structure of the actuator straightens out, and shear strain is applied to its surface (Figure 3a; Figure S19, Supporting Information). This shear stress leads to cracking in the Ag-rich shell layer, thereby increasing the electrical resistance

www.small-journal.com

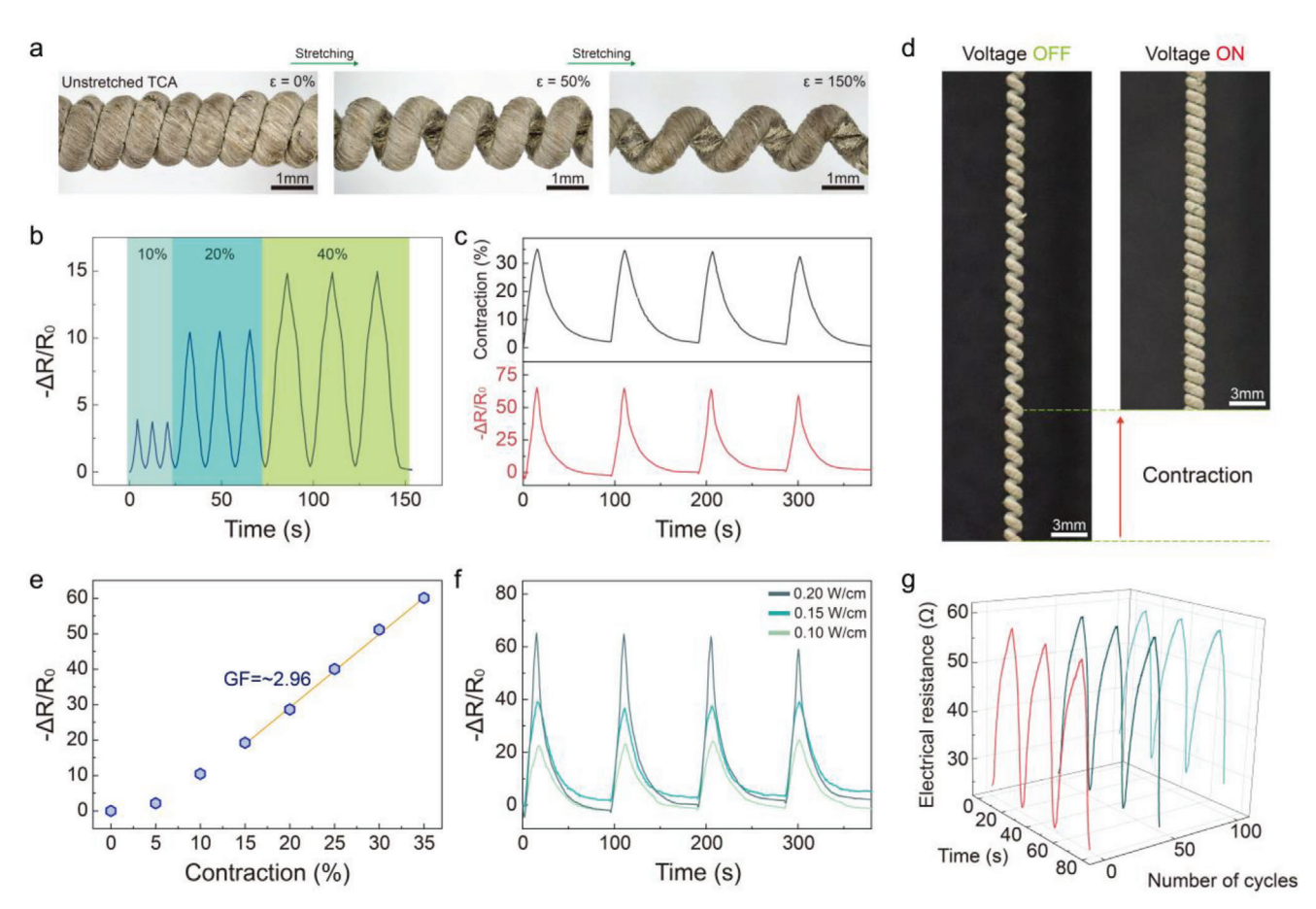


**Figure 3.** a) Digital microscopic images of the proprioceptive fiber actuator at applied tensile strains of 0, 50, and 150%. b) Relative change in the electrical resistance of the proprioceptive fiber actuator upon repeated tensile strains of 10, 20, and 40%. c) Contractile strain of the proprioceptive fiber actuator under repeated applications of external power at 0.2 W cm<sup>-1</sup> and the corresponding resistive response of the fiber actuator. d) Photographs showing the change in the coiled structure of the proprioceptive fiber actuator under payloads before and after the application of external voltage. e) Variation in the normalized electrical resistance of the proprioceptive fiber actuator as a function of contractile strain. f) Resistive response of the proprioceptive fiber actuator during repeated contractile actuations under external powers of 0.1, 0.15, and 0.2 W cm<sup>-1</sup>. g) Changes in the electrical resistance of the proprioceptive fiber actuator over 100 cycles of repeated contractile actuations, using an external power of 0.15 W cm<sup>-1</sup> and a payload of 0.8 N.

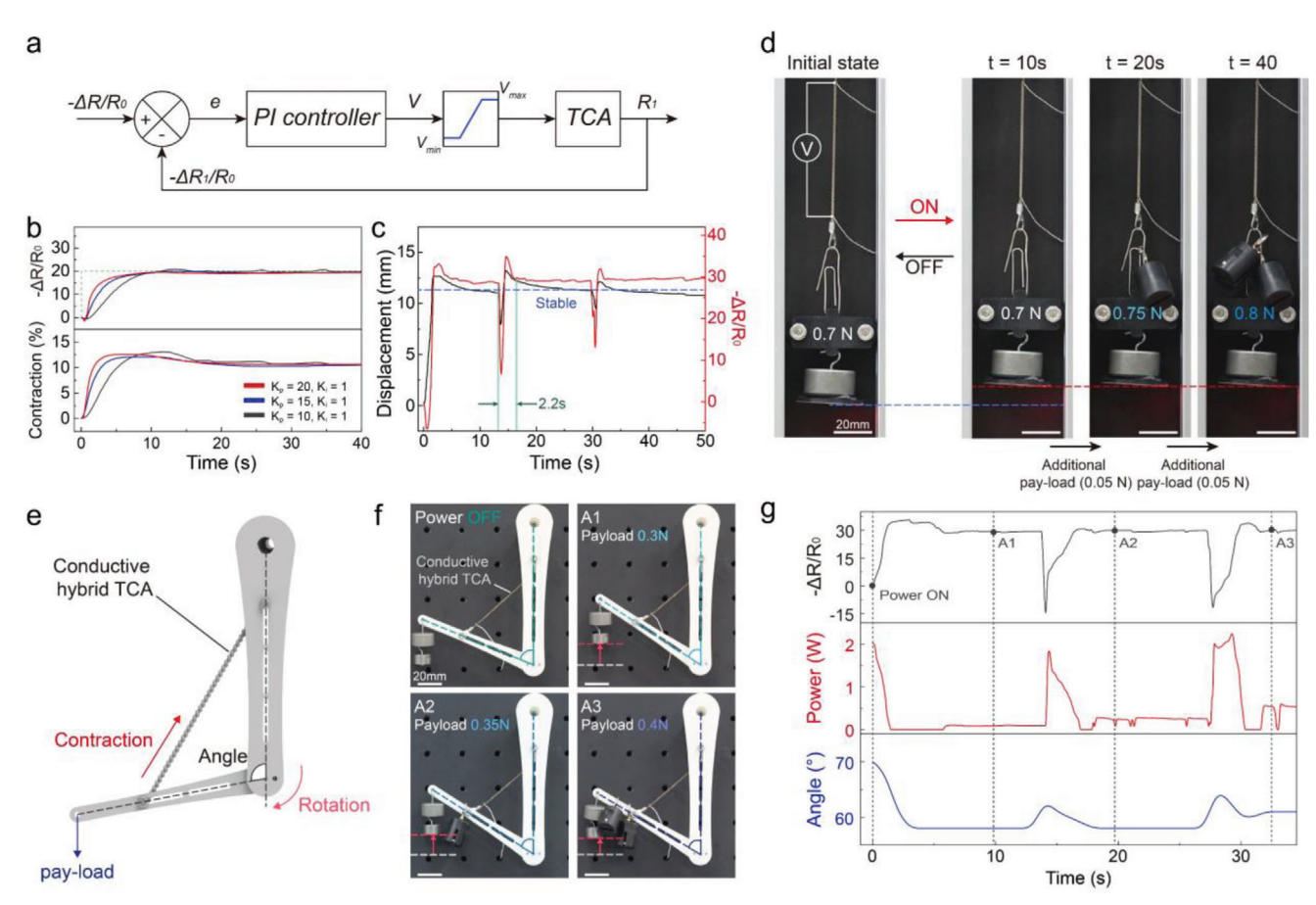
of the fiber actuator.<sup>[47]</sup> Figure 3b illustrates the relative change in the electrical resistance of the fiber actuator under repeated tensile strains of 10%, 20%, and 40%, displaying stable and distinguishable responses with high repeatability. The fabricated proprioceptive fiber actuator exhibited a fast response time (≈240 ms) and recovery time (≈340 ms) for strain sensing under a tensile strain of 5% (Figure \$20, Supporting Information). In addition, the fiber actuator demonstrated a stable response during repeated stretch-release cycles at 40% across different stretching rates (Figure S21, Supporting Information). Based on the stable response of the fiber actuator, it exhibited negligible hysteresis in its resistive response during consecutive stretchrelease cycles across various strain ranges of 10%, 20%, and 30% (Figure S22, Supporting Information). This resistive response under mechanical deformation can be leveraged to continuously monitor the actuator's contractile actuation, thus denoting the fiber actuator's proprioceptive sensing capability.

Figure 3c demonstrates the resistive response of the fiber actuator (fabricated using a 1.2 N coiling load) during repeated con-

tractile actuations under a payload of 0.7 N and external power of 0.2 W cm<sup>-1</sup>. The fiber actuator exhibits a negative resistive response under contractile actuation, which can be attributed to the efficient recovery of the initial coiled structure of the actuator (Figure 3d). In addition, we analyzed the stress distribution of the fiber actuator during contractile actuation via a numerical simulation. The results demonstrate the effective release of mechanical stress applied to the fiber actuator following its contractile actuation (Figure S23, Supporting Information). Figure 3e displays the relative change in the electrical resistance of the fiber actuator (fabricated using a 1.2 N coiling load) in relation to contractile actuation under a payload of 0.7 N. The proprioceptive fiber actuator exhibited a linear response in the negative direction as the contractile strain increased. The gauge factor (GF) of the fiber actuator's proprioceptive sensing, defined as  $GF = \delta((R-1))$  $R_0/R_0/\delta\epsilon$  where R and  $R_0$  indicate the electrical resistance of the loaded fiber actuator with and without applied power, and  $\epsilon$ is the contractile strain of the fiber actuator with a payload and external power, was calculated to be ≈2.96 for the contractile strain



www.small-journal.com



**Figure 4.** a) Schematic block diagram of the closed-loop feedback control system for the proprioceptive fiber actuator. b) The relative resistive response and the displacement of proprioceptive fiber actuator with various proportional gain ( $K_p = 10$ , 15, 20) c) The relative resistive response and the displacement of proprioceptive fiber actuator under additional payload from 0.7 to 0.8 N loading with closed-loop feedback control system. d) Photograph of proprioceptive fiber actuator under additional payload loading with the closed-loop feedback control system from 0.7 to 0.8 N. e) Schematic illustration of artificial arm system generated by conductive hybrid TCA. f) Photograph of the artificial arm system upon adding the payload from 0.3 to 0.4 N. g) The relative resistive response, the electrical power, and angle change of proprioceptive fiber actuator under additional payload from 0.3 to 0.4 N using the closed-loop feedback control system.

range of 15 to 35%. The proprioceptive fiber actuator not only exhibits actuation performances but also demonstrates sensing performances superior to those of previously reported fiber actuators (Table S1, Supporting Information).

Owing to the high stability and repeatability of the proprioceptive sensing, the fiber actuator also showed a stable response for various repeated contraction strains actuated using external powers of 0.1, 0.15, and 0.2 W cm $^{-1}$  (Figure 3f). The stable resistive response of the proprioceptive sensing was successfully maintained without considerable degradation, even after an intensive 100-cycle test with an external power of 0.15 W cm $^{-1}$ , demonstrating the high durability of the proprioceptive fiber actuator, as shown in Figure 3g.

#### 2.4. Demonstration of the Resistance Feedback Control Loop

Based on the proprioceptive sensing capability of the fiber actuator, we have successfully designed a robust closed-loop feedback controller. The controller consists of Proportional-Integral (PI)

control and a feedback loop, as illustrated in Figure 4a. To achieve the target displacement of the fiber actuator, we measured the relative resistance change of the fiber actuator to calculate the error, which is obtained by subtracting the output value ( $\Delta R_1/R_0$ ) from the target value  $(\Delta R/R_0)$  in real-time during operation. Simultaneously, the system compensates the input voltage to reduce the error. Figure 4b displays the step response of the proprioceptive fiber actuator upon increasing the proportional gain (K<sub>n</sub>) from 10 to 20 with a 0.8 N payload and target relative resistance change of 20. Additionally, an integral controller  $(K_i = 1)$  was used to overcome the steady-state error. With the increase in K<sub>n</sub>, the time constant, which is the time it takes for the step response to reach 63% of its target value, decreased from 3 to 2.05 s, showing a fast response time of the proprioceptive fiber actuator (Video S2, Supporting Information). Moreover, the fiber actuator could be successfully contracted for various setpoints of relative resistance change from 30 to 50 by compensating the input, demonstrating a fast response time (Figure S24, Supporting Information).

To verify the stability of the proprioceptive fiber actuator with the closed-loop feedback controller, additional external weights



We demonstrated the potential of this proprioceptive fiber actuator in paving the way for the creation of feedback-regulated artificial muscles with both high performance and low operation temperature.

were applied to the fiber actuator during operation with a 0.7 N payload and a target relative resistance change of 30 (Figure 4c; Video \$3, Supporting Information). When an external load of 0.05 N (5 g) was additionally applied to the fiber actuator, it temporarily straightened, leading to a considerable change in the resistive response of the fiber actuator. To restore the target displacement, the controller immediately compensated the electrical input power to the fiber actuator until the relative resistance change of the actuator reached the target value (Figure \$25, Supporting Information). Thanks to the robust control system, relative resistance change was rapidly returned to the target value ( $-\Delta R_1/R_0 = 30$ ) in 2.2 s, resulting in the fiber actuator returning to its target displacement. Therefore, the proprioceptive fiber actuator could stably maintain its target displacement without considerable elongation, even when external loads of 0.05 N were additionally weighed into the fiber actuator (Figure 4d).

Furthermore, we chose to demonstrate the presented proprioceptive fiber actuator as an artificial muscle for an artificial arm system. As shown in Figure 4e, an artificial arm system could generate a folding motion owing to the contraction of the fiber actuator, and as a result, the system could lift the payload which is suspended at the end of the arm. The fabricated artificial arm system successfully generated the folding motion with a 0.3 N payload using the closed-loop feedback control system as well as the angle of the artificial arm system (\$\approx 58\circ\) could be steadily retained despite the external loads being added, ranging from 0.3 to 0.4 N (Figure 4f; Video S4, Supporting Information). When the additional loads were applied to the artificial arm system, the control system compensated the electrical input power to maintain the contractile actuation of the fiber actuator, resulting in the maintenance of the artificial arm's angle (Figure 4g; Video S4, Supporting Information).

#### 3. Conclusion

In conclusion, we have successfully developed a proprioceptive electrothermal fiber actuator with high actuation performance, low operational temperature, and inherent self-sensing capabilities. The proprioceptive fiber actuator was prepared by fabricating a non-conductive hybrid TCA using the twisting and coiling process of PE and PU fibers and by embedding a significant quantity of AgNPs into the PU fibers in the TCA. The Agrich shell conductive region in the fiber actuator allows the actuator to efficiently generate Joule heat under an external voltage, obviating the need for bulky external heat sources. The fabricated fiber actuator achieved a remarkable contractile actuation of  $\approx$ 36% at an impressively low operational temperature of ≈83 °C. Comprehensive studies, including experimental data, mathematical analyses, and numerical simulations, highlighted the actuator's effective heat dissipation and rapid relaxation capabilities under natural cooling conditions, mainly attributed to the Ag-rich shell region. Furthermore, real-time monitoring of the actuator's contractile actuation was achieved by measuring the changes in its electrical resistance. Leveraging its proprioceptive sensing properties, the fiber actuator can be controlled to retain its intended contractile behavior, even in the face of external perturbations, via a closed-loop feedback control system.

#### 4. Experimental Section

Preparation of Non-Conductive Hybrid TCA: Two strands of Highdensity polyethylene (HDPE) fibers (Yafo Co., Ltd, PE braided line, 0.148 mm) were prepared, each having a length 2.2 times greater than that of the polyurethane-based stretchable spandex fibers (Hyosung Co., Ltd., Creora, 280 denier). Subsequently, one end of each of the two HDPE fibers were fixed with 20 spandex fibers to a custom-made twisting machine. The other ends of the HDPE fibers and spandex fibers, pre-stretched to have the same length with the HDPE fibers (a pre-strain of 220%), were fixed using a distance holder. The pre-stretched spandex fibers and HDPE fibers were twisted with 205 turns using the custom-made twisting machine. This twisting procedure caused the pre-stretched spandex fibers to envelop the HDPE fibers in a cylindrical arrangement, all the while maintaining the initial length of the HDPE fibers. Upon completion of the twisting process, the distance holder was removed, and an isobaric payload was applied to the twisted fibers. Additional rotations were then introduced to the fibers under this isobaric load, which transformed their twisted configuration into a coiled structure. This transformation resulted in a twisted and coiled structure of the fibers. The number of rotations applied to the fibers to create the coiling structure of the TCA depends on the coiling load used in the fabrication process. In this work, 280 turns were used for a coiling load of 1.2N. To ensure the stability of this configuration, the affixed fibers underwent an annealing process at 150 °C for an hour. Following this, the fibers were allowed to cool down at room temperature (25  $^{\circ}$ C) for an hour, in order to stabilize the polymer structure.

Fabrication Process of AgNPs-Based Conductive Hybrid TCA: The AgNPs-based conductive hybrid TCA, also known as a proprioceptive fiber actuator, was fabricated by incorporating an abundant amount of AgNPs into the PU fibers in the non-conductive hybrid TCA. The AgNPs were embedded into the PU fibers through a chemical reduction process, which included absorbing Ag+ ions into the PU fiber matrix, followed by reducing these absorbed Ag+ ions into AgNPs. To enable the absorption of a large quantity of Ag+ ions into the PU fiber matrix, the fabricated non-conductive hybrid TCA was immersed in an AgCF3COO (silver trifluoroacetate) (Sigma-Aldrich Corp., 98%, T62405) solution in ethyl alcohol anhydrous (35wt%) (Daejung Co., Ltd., 99.9%, CAS 64-17-5) for 20 min. After the absorption process, the TCA was dried at room temperature for 10 min. Before reducing the Ag+ ions within the PU matrix, the non-conductive hybrid TCA, containing Ag+ ions, was stretched out with 50% tensile strain to allow dense formation of the AgNPs between the adjacent coil structures in the fiber actuator. The stretched nonconductive hybrid TCA, containing Ag+ ions, was then immersed in an ascorbic acid solution (Sigma Aldrich corp., (BioXtra) 99.0%, A5960) in DI water (4 wt%) to directly reduce the Ag+ ions into AgNPs within the PU fiber matrix. After 1 h, the reducing agent was rinsed off the surface of the fiber actuator with DI water, and the actuators were left to completely air-dry. This chemical reduction process was repeated over 3 cycles, to ensure a high electrical conductivity in the conductive hybrid TCA.

Characterization of the Proprioceptive Fiber Actuator: SEM images were captured using a typical scanning electron microscope (Hitachi Inc., S-4800) to visualize the surface morphology of the AgNPs-based conductive hybrid TCA, a proprioceptive fiber actuator. For high-resolution photographs of the proprioceptive fiber actuator, a digital microscope (KEYENCE Ltd., VHX-6000) was utilized. The weight fraction of AgNPs in the fiber actuator was measured using thermogravimetric analysis equipment (TA Instruments Inc., Auto Q500). Real-time measurements of the surface temperature changes and IR images during the electrothermal contractile actuation of the actuator were carried out using an infrared temperature measurement microscope system (Teledyne FLIR LLC., ETS320). To assess the mechanical stiffness of various proprioceptive fiber

SMQ

www.small-journal.com

actuators, a custom-made stretching machine, consisting of a force-meter (Imada Inc., DSV-2N) and a linear x-stage (SCIENCETOWN Inc., SM1-0810-3S), was employed with a stretching speed of 0.1 mm s $^{-1}$ . The displacement of the fiber actuator during contractile actuation was measured using a non-contact laser displacement sensor (Optex fa Co., Ltd, CD22-100-485) through RS485 communication using a customized Python program. To enhance data accuracy, a 1D median filter was applied to eliminate any noise interference during the data acquisition process. To supply constant electrical power to the proprioceptive fiber actuator for its contractile actuation, a programmable source meter (Keithley Instruments Inc., Source meter 2450) was used. The input voltage was controlled in real-time based on the measured electrical resistance using a customized Python program.

Finite Element Method Simulation: The finite element method (FEM) simulation, which explains the transient thermal behavior of the AgNPsbased TCA, was carried out using 3D modeling in simulation software (ANSYS, ANSYS R17.2). The geometrical model of the AgNPs-based TCA was designed with a self-coiled structure using SolidWorks 2016. This geometrical model, a self-coiled structure, was then imported into ANSYS with the physical dimensions of the AgNPs-based TCA. The structural parameters used for the AgNPs-based TCA were as follows: outer diameter = 1.5 mm, wire diameter = 0.7 mm, PE core radius = 0.21 mm, thickness of the Ag-concentrated layer =  $6.3 \mu m$  (derived from Equations S1 and S2, Supporting Information), number of coil structure turns = 5, and pitch of the coil structure = 1.3 mm. The material properties of Ag-concentrated layer were as follows: Density =  $10.49 \text{ g cm}^{-3}$ , Thermal conductivity = 429 W m  $K^{-1}$ , and Specific heat = 237 J kg<sup>-1</sup>•K. Similarly, the material properties used for the PE core fiber were as follows: Density =  $0.95 \text{ g cm}^{-3}$ , Thermal conductivity = 0.51 W m<sup>-1</sup>•K, and Specific heat = 2000 J kg<sup>-1</sup>•K. Likewise, the material properties used for the PU fibers were as follows: Density =  $1.35 \text{ g cm}^{-3}$ , Thermal conductivity =  $0.0204 \text{ W m}^{-1} \cdot \text{K}$ , and Specific heat = 1000 J kg<sup>-1</sup>•K. One specific boundary condition was applied to the AgNPs-based TCA: The temperature of the TCA changes from 80 °C to room temperature, with the temperature-dependent coefficient of convection. The initial temperature of the AgNPs-based TCA (measured as 80  $^{\circ}$ C by IR imaging) was set as the temperature of the contracted TCA immediately after the applied voltage was turned off. The convection coefficient was calculated upon varying temperatures using Equation S7 (Supporting Information) in MATLAB R2021a and then applied to the surface of the Ag-concentrated layer.

Finite Element Method Simulation Regarding the Stress Distribution of Fiber Actuator: The finite element method (FEM) simulation, which explains the stress response of the AgNPs-based TCA during contractile actuation, was carried out based on 3D modeling using a COMSOL Multiphysics (version 6.0, https://www.comsol.com). The proprioceptive fiber actuator was modeled as a self-coiled structure. Furthermore, the structure of the fiber actuator was divided into an Ag-concentrated layer, a PU layer, and an HDPE fiber, as shown in Figure S23 (Supporting Information). The structural parameters used for the AgNPs-based TCA were as follows: outer diameter = 1.5 mm, wire diameter = 0.7 mm, PE core radius = 0.21 mm, the thickness of the Ag-concentrated layer = 6.3 um, number of coil structure turns = 5, and pitch of the coil structure = 1.3 mm. The material properties of the Ag-concentrated layer were as follows: Density =  $10.49 \text{ g cm}^{-3}$ , Poisson's ratio = 0.49, Elastic modulus = 81.1 GPa. Similarly, the material properties used for the PU layer were as follows: Density =  $0.135 \text{ g cm}^{-3}$ , Poisson's ratio = 0.49, Elastic modulus = 6 MPa. Likewise, the material properties used for the HDPE core fiber were as follows: Density =  $0.95 \text{ g cm}^{-3}$ , Poisson's ratio = 0.49, Elastic modulus = 1,000 MPa. The boundary condition was specified at the AgNPsbased TCA: The contractile actuation of the fiber electrode changes to 30% from the initial state. The z-axis was fixed during the contractile actuation of the fiber actuator.

#### **Supporting Information**

Supporting Information is available from the Wiley Online Library or from the author.

#### Acknowledgements

S.N. and J.K. contributed equally to this work. This work was supported by the National Research Foundation of Korea (NRF) grant funded by the Korea government (MSIT) (No. NRF-2021R1C1C1009271 and NRF-2022R1A4A3033320). This research was also supported by the Development of technologies for electroceuticals of the National Research Foundation (NRF) funded by the Korean government (MSIT) (No. NRF-2022M3E5E9017837). This work was supported by the Industrial Fundamental Technology Development Program (20018274, Development of gripper system for various production processes and multi-modal flexible tactile sensor system) funded by the Ministry of Trade, Industry & Energy (MOTIE) of Korea. Finally, this work was supported by the Korea Medical Device Development Fund grant funded by the Korea government (the Ministry of Science and ICT, the Ministry of Trade, Industry and Energy, the Ministry of Health & Welfare, the Ministry of Food and Drug Safety) (Project Number: 1711196794, RS-2023-00243310).

#### **Conflict of Interest**

The authors declare no conflict of interest.

#### **Data Availability Statement**

The data that support the findings of this study are available from the corresponding author upon reasonable request.

#### Keywords

artificial muscle, closed-loop feedback control, fiber actuators, proprioceptive sensing, twisted and coiled actuators

Received: October 18, 2023 Revised: January 4, 2024 Published online: March 29, 2024

- [1] C. Majidi, Adv. Mater. Technol. 2019, 4, 1800477.
- [2] H. Huang, Y. Lyu, K. Nan, Soft Matter 2023, 19, 1269.
- [3] M. Manti, T. Hassan, G. Passetti, N. D'Elia, C. Laschi, M. Cianchetti, Soft Robot 2015, 2, 107.
- [4] X. Liu, M. Song, Y. Fang, Y. Zhao, C. Cao, Adv. Intell. Syst. 2022, 4, 2100128
- [5] P. Ohta, L. Valle, J. King, K. Low, J. Yi, C. G. Atkeson, Y. L. Park, Soft Robot 2018, 5, 204.
- [6] M. E. Giannaccini, C. Xiang, A. Atyabi, T. Theodoridis, S. Nefti-Meziani, S. Davis, Soft Robot 2018, 5, 54.
- [7] I. H. Kim, S. Choi, J. Lee, J. Jung, J. Yeo, J. T. Kim, S. Ryu, S. kyun Ahn, J. Kang, P. Poulin, S. O. Kim, Nat. Nanotechnol. 2022, 17, 1198.
- [8] G. M. Whitesides, Angew. Chem., Int. Ed. 2018, 57, 4258.
- [9] R. Yin, B. Yang, X. Ding, S. Liu, W. Zeng, J. Li, S. Yang, X. Tao, Adv. Mater. Technol. 2020, 5, 2000341.
- [10] O. Kilic Afsar, A. Shtarbanov, H. Mor, K. Nakagaki, J. Forman, K. Modrei, S. H. Jeong, K. Hjort, K. Höök, H. Ishii, UIST '21: The 34th Annual ACM Symposium on User Interface Software and Technology, Association for Computing Machinery, NY USA 2021, 1010.
- [11] T. L. Buckner, R. A. Bilodeau, S. Y. Kim, R. Kramer-Bottiglio, *Proc. Natl. Acad. Sci. USA* 2020, 117, 25360.
- [12] S. Si, C. Sun, J. Qiu, J. Liu, J. Yang, Appl. Mater. Today **2022**, 27, 101508.
- [13] J. Foroughi, G. M. Spinks, S. Aziz, A. Mirabedini, A. Jeiranikhameneh, G. G. Wallace, M. E. Kozlov, R. H. Baughman, ACS Nano 2016, 10, 9129.

**ADVANCED** SCIENCE NEWS

www.advancedsciencenews.com



- [14] P. T. Phan, M. T. Thai, T. T. Hoang, J. Davies, C. C. Nguyen, H. P. Phan, N. H. Lovell, T. N. Do, Sci. Rep. 2022, 12, 11067.
- [15] T. Jia, Y. Wang, Y. Dou, Y. Li, M. Jung de Andrade, R. Wang, S. Fang, J. Li, Z. Yu, R. Qiao, Z. Liu, Y. Cheng, Y. Su, M. Minary-Jolandan, R. H. Baughman, D. Qian, Z. Liu, Adv. Funct. Mater. 2019, 29, 18082412.
- [16] N. Sheng, Y. Peng, F. Sun, J. Hu, Adv. Fiber Mater. 2023, 5, 1534.
- [17] Y. Yu, J. Wang, X. Han, S. Yang, G. An, C. Lu, Adv. Fiber Mater. 2023, 5. 868.
- [18] S. J. Park, K. Choi, H. Rodrigue, C. H. Park, Sci. Rep. 2022, 12, 11398.
- [19] A. Maziz, A. Concas, A. Khaldi, J. Stålhand, N. K. Persson, E. W. H. Jager, Sci. Adv. 2017, 3, 1600327.
- [20] P. T. Phan, T. T. Hoang, M. T. Thai, H. Low, N. H. Lovell, T. N. Do, Soft Robot 2022, 9, 820.
- [21] M. Li, Y. Tang, R. H. Soon, B. Dong, W. Hu, M. Sitti, Sci. Adv. 2022, 8, 5616.
- [22] M. Kanik, S. Orguc, G. Varnavides, J. Kim, T. Benavides, D. Gonzalez, T. Akintilo, C. Cem Tasan, A. P. Chandrakasan, Y. Fink, P. Anikeeva, Science (80-.) 2019, 365, 145.
- [23] D. Kongahage, A. Ruhparwar, J. Foroughi, Adv. Mater. Technol. 2021, 6, 2000894.
- [24] X. Leng, G. Mei, G. Zhang, Z. Liu, X. Zhou, Chem. Soc. Rev. 2023, 52, 2377.
- [25] L. Xu, Q. Peng, Y. Zhu, X. Zhao, M. Yang, S. Wang, F. Xue, Y. Yuan, Z. Lin, F. Xu, X. Sun, J. Li, W. Yin, Y. Li, X. He, *Nanoscale* 2019, 11, 8124.
- [26] Y. Wang, Y. Zhao, M. Ren, Y. Zhou, L. Dong, X. Wei, J. He, B. Cui, X. Wang, P. Xu, J. Di, Q. Li, Nano Energy 2022, 102, 107609.
- [27] X. Hu, R. Liu, K. Zhao, Y. Wang, X. Bao, L. Xu, G. Cheng, J. Ding, J. Bionic. Eng. 2023, 20, 1626.
- [28] W. He, Z. Ge, W. Kong, L. Ye, Z. Zhang, X. Zhao, W. Lin, G. Wang, ACS Sustainable Chem. Eng. 2022, 10, 15186.
- [29] C. Piao, H. Jang, T. G. Lim, H. Kim, H. R. Choi, Y. Hao, J. W. Suk, Compos. Part B Eng. 2019, 178, 107499.
- [30] J. Van Der Weijde, H. Vallery, R. Babuška, Soft Robot 2019, 6, 621.
- [31] P. Zhao, B. Xu, Y. Zhang, B. Li, H. Chen, ACS Appl. Mater. Interfaces 2020, 12, 15716.
- [32] J. Sun, B. Tighe, Y. Liu, J. Zhao, Soft Robot 2021, 8, 213.
- [33] C. S. Haines, N. Li, G. M. Spinks, A. E. Aliev, J. Di, R. H. Baughman, Proc. Natl. Acad. Sci. U.S.A. 2016, 113, 11709.

- [34] C. S. Haines, M. D. Lima, N. Li, G. M. Spinks, J. Foroughi, J. D. W. Madden, S. H. Kim, S. Fang, M. J. De Andrade, F. Göktepe, Ö. Göktepe, S. M. Mirvakili, S. Naficy, X. Lepró, J. Oh, M. E. Kozlov, S. J. Kim, X. Xu, B. J. Swedlove, G. G. Wallace, R. H. Baughman, *Science* 2014, 343, 868.
- [35] H. Kim, J. H. Moon, T. J. Mun, T. G. Park, G. M. Spinks, G. G. Wallace, S. J. Kim, ACS Appl. Mater. Interfaces 2018, 10, 32760.
- [36] J. Chen, M. Xu, E. Pakdel, W. Zhong, X. Li, L. Sun, D. Wang, Sensors Actuators A Phys. 2022, 346, 113822.
- [37] Y. Song, S. Zhou, K. Jin, J. Qiao, D. Li, C. Xu, D. Hu, J. Di, M. Li, Z. Zhang, Q. Li, *Nanoscale* 2018, 10, 4077.
- [38] M. Hiraoka, K. Nakamura, H. Arase, K. Asai, Y. Kaneko, S. W. John, K. Tagashira, A. Omote, Sci. Rep. 2016, 6, 36358.
- [39] D. Zhou, W. Zuo, X. Tang, J. Deng, Y. Liu, Bioinspir. Biomim. 2021, 16, 045003.
- [40] S. Wang, H. Huang, H. Huang, B. Li, K. Huang, IEEE Robot. Autom. Lett. 2021, 6, 2775.
- [41] S. Liu, X. Tang, D. Zhou, Y. Liu, Sensors Actuators A Phys. 2020, 315, 112292.
- [42] S. Y. Yang, K. H. Cho, Y. Kim, M. G. Song, H. S. Jung, J. W. Yoo, H. Moon, J. C. Koo, J. Do Nam, H. R. Choi, Smart Mater. Struct. 2017, 26, 105025
- [43] K. Kim, K. H. Cho, H. S. Jung, S. Y. Yang, Y. Kim, J. H. Park, H. Jang, J. Do Nam, J. C. Koo, H. Moon, J. W. Suk, H. Rodrigue, H. R. Choi, Adv. Eng. Mater. 2018, 20, 1800536.
- [44] M. Suzuki, N. Kamamichi, Smart Mater. Struct. 2018, 27.
- [45] K. Masuya, S. Ono, K. Takagi, K. Tahara, IEEE Robot. Autom. Lett. 2018. 3, 1824.
- [46] H. Kim, A. Shaqeel, S. Han, J. Kang, J. Yun, M. Lee, S. Lee, J. Kim, S. Noh, M. Choi, J. Lee, ACS Appl. Mater. Interfaces 2021, 13, 39868.
- [47] J. Lee, S. Shin, S. Lee, J. Song, S. Kang, H. Han, S. Kim, S. Kim, J. Seo, D. Kim, D. Kim, T. Lee, ACS Nano 2018, 12, 4259.
- [48] B. Yu, Q. Gu, G. Hu, T. Yang, M. Liu, H. Shi, Z. Xiang, T. Huang, M. Zhu, H. Yu, Chem. Eng. J. 2024, 480, 148058.
- [49] O. H. Fred-Ahmadu, G. Bhagwat, I. Oluyoye, N. U. Benson, O. O. Ayejuyo, T. Palanisami, *Sci. Total Environ.* 2020, 706, 135978.
- [50] S. Yao, J. Wang, X. Liu, Int. J. Therm. Sci. 2021, 165, 106927.
- [51] X. Lu, Y. Zhang, S. Xiao, Y. Zhao, J. Li, J. Zhou, Q. Ouyang, Appl. Therm. Eng. 2022, 204, 118031.